The evolution and dynamics of the Hunga ~~Tonga~~ Tonga-Hunga Ha’apai plume in the stratosphere: progressing aerosol properties and vertical separation from the water vapour

Bernard Legras[1], Clair Duchamp[1], Pasquale Sellitto[2,3], Aurélien Podglajen[1], Elisa Carboni[4], Richard Siddans[4], Jens-Uwe Grooß[5], Sergey Khaykin[6], and Felix Ploeger[5]

[1]Laboratoire de Météorologie Dynamique (LMD-IPSL), UMR CNRS 8539, ENS-PSL, École Polytechnique, Sorbonne Université, Institut Pierre Simon Laplace, Paris, France
[2]Univ. Paris Est Créteil and Université de Paris Cité, CNRS, Laboratoire Interuniversitaire des Systèmes Atmosphériques (LISA-IPSL), Institut Pierre-Simon Laplace, Créteil, France
[3]Istituto Nazionale di Geofisica e Vulcanologia (INGV), Osservatorio Etneo (OE), Catania, Italy
[4]UK Research and Innovation, Science and Technology Facilities Council, Rutherford Appleton Laboratory, Chilton, UK
[5]Institute for Energy and Climate Research: Stratosphere (IEK–7), Forschungszentrum Jülich, Jülich, Germany
[6]Laboratoire Atmosphères, Milieux, Observations Spatiales (LATMOS-IPSL), UMR CNRS 8190, Institut Pierre Simon Laplace, Sorbonne Univ./UVSQ, Guyancourt, France

Correspondence: Bernard Legras (bernard.legras@lmd.ipsl.fr)

Abstract. We use a combination of space-borne instruments to study the unprecedented stratospheric plume after the ~~Hunga~~ Tonga eruption of 15 January 2022. The plume was formed of two initial clouds at 30 and 28 km mostly composed of sub-micronic sulphate particles without ashes, washed-out within the first hours. The large amount of water vapour injected led to a fast conversion of SO_2 to sulphates and induced a descent of the plume over the first three weeks by radiative cooling. ~~While~~ Whereas SO_2 has returned to background levels by the end of January, the sulphate plume persisted ~~until June~~for the next 6 months, mainly confined between 20°N and 35°S until June due to the zonal symmetry of the summer stratospheric circulation at 24-25 km. As sulphate particles grew through hydration and coagulation, they sediment and separate from the equally persistent and ascending moisture entrained in the Brewer-Dobson circulation. Sulphate aerosol optical depths derived from the IASI infared sounder show that during the first two months the aerosol plume was not simply diluted and dispersed passively but rather organized in concentrated patches. ~~Winds from the space-borne Doppler lidar ALADIN/AEOLUS~~ Space-borne lidar winds suggest that those structures, generated by shear-induced instabilities, are associated with vorticity anomalies. They likely enhance the duration and impacts of the plume.

1 Introduction

The phreato-magmatic eruption of the Hunga Tonga-Hunga Ha’apai (hereafter ~~Hunga Tonga~~HTHH) of 15 January 2022 is exceptional in several respects. Its explosive intensity is close to that of the eruption of Mount Pinatubo in 1991, with a Volcanic Explosivity Index of ∼6 (Poli and Shapiro, 2022). The induced atmospheric Lamb wave circled the globe at least 4 times with an amplitude ~~unseen since~~ comparable to that of the 1883 Krakatau eruption ~~(Matoza et al., 2022; Vergoz et al., 2022)~~

(Matoza et al., 2022; Vergoz et al., 2022; Wright et al., 2022). Within a few hours, several successive events injected material up to the mesosphere ~~(Podglajen et al., 2022)~~, with the bulk of the plume being detrained between 26 and 34 km ~~(Carr et al., 2022)~~ (Carr et al., 2022; Khaykin et al., 2022; Podglajen et al., 2022; Proud et al., 2022; Taha et al., 2022). A further remarkable fact is that the plume carried an unprecedented amount of water vapour into the stratosphere, increasing instantaneously its overall water vapour content by $\sim$10% ~~(Millán et al., 2022)~~(Millán et al., 2022; Khaykin et al., 2022). Quite surprisingly, the ~~first~~ satellite data gathered after the event reported a stratospheric SO_2 injection of only 0.5 Tg, on par with much smaller and less explosive eruptions (Millán et al., 2022; **?**). This led to an early estimate of negligible climatic impact ~~(Witze, 2022)~~ (Witze, 2022; Zhang et al., 2022). Here, we report on the evolution of the stratospheric plume during the first months after the eruption and we advocate that its climatic effect is very significant due to the amount of water vapour and of the sulphate aerosols which have resulted from a fast conversion. We focus on the circumnavigation of the plume and proceed from the large-scale to the local patterns.

2 ~~The mean~~ Six-month evolution of the zonal ~~pattern~~mean

Figure A1 shows the zonal mean stratospheric conditions in January-March. In the domain 21-28 km and 25°S-15°N, they are characterized by an easterly band with a maximal angular speed of 30°/day at 25 km and 5°S. The diabatic heating rate is positive everywhere except a narrow region near 27 km over the equator (Fig. A1b). These conditions are stable during the whole January-March period (Fig. A1d-g). In April-June, the rotation weakens and changes sign (Fig. A1d&f) while the warming turns to cooling (Fig. A1e&g) as a combined effects of the Quasi Biennial Oscillation (QBO) and the seasonal cycle.

Figure 1 shows that after an initial ~~fast latitudinal dispersion , the plume stays~~ rapid meridional dispersion in the first days after the eruption (Khaykin et al., 2022), the aerosol and water plume stay mostly confined within the band 35°S-20°N until June when wave activity increases, and evolves slowly in the zonal mean. By mid-February, ~~the plume has already spread all around the Earth. However, the the~~ aerosols and water vapour have already spread through all longitudes (Khaykin et al., 2022, , and Sec. 4 below). The Ozone Mapping and Profiler Suite Limb Profiler (OMPS-LP) extinction ratio increases in time at the core of the cloud ~~increases in time~~ and reaches an ~~April maximum. Meanwhile,~~ a mid-April maximum. The simultaneous increase of the Cloud-Aerosol Lidar with Orthogonal Polarisation (CALIOP) scattering ratio ~~decreases. This~~ suggests particle growth. The Microwave Limb Sounder (MLS) water vapour initially correlates very well with the aerosols but they progressively move apart vertically (see also Schoeberl et al., 2022). By early June, aerosols and moisture appear fully separated, respectively below and above 25 km. The limb instruments suggest larger vertical plume extension than CALIOP ~~due~~ owing to the resolution and effects of the Earth curvature in the viewing geometry (Gorkavyi et al., 2021).

The plume vertical motion~~calculated as described in Appendix A3~~, calculated following Appendix A3, is analysed (Fig. 2) for two latitude ranges and the apparent aerosol radius is estimated by interpreting ~~this~~ the aerosol plume motion as a fall speed of the scattering particles using Eq. (9.42) of Seinfeld and Pandis (2016). ~~Two separate descent regimes are identified from observations~~The descent of aerosols separates in two subsequent phases. For the first phase, Figure 2b and d-e show an initial fast descent until ~~mid-February~~about 20 February in the two latitude bands, which would imply unrealistically large aerosol sizes. The water vapour follows the aerosol downward motion, ~~against the rising ERA5 motion~~ in contrast to the rising motion in ERA5. Sellitto et al. (2022) (S2022 hereafter) explain this ~~discrepancy~~ behaviour by the cooling effect of water vapour infrared emission which is unaccounted for in ERA5, and ends when the water plume gets diluted and approaches vertically its neutral radiative level.

In the second phase, the diluted water vapour is ~~rising in agreement with~~ ascending at the same rate as ERA5 upwelling, while the aerosols continue their descent, though at a reduced speed. The descent with respect to the ERA5 air is now compatible with a realistic ~~aerosol size, which is much smaller and growing~~ and growing aerosol size. Figure 2e suggests that the aerosol size after growing up to about 1.5~~-2~~ µm in ~~April~~ April-May starts shrinking in ~~May~~May-June.

The extinction-to-backscatter ratio, obtained by combining OMPS-LP and CALIOP data, is shown in Fig. 2g. This parameter is also computed using a Mie code (Fig. 2f). The observed trend of the extinction-to-backscatter ratio with aerosol size is consistent with the theoretical trend direction for sizes between 1 and 2 µm. Considering that the extinction saturates and decays (Fig. 2a) and the decoupling between the aerosols and moisture, we suggest that the initial growth of the particles was by hydration until ~~mid-March~~April, where the extinction culminates and was followed by coagulation growth over April-May and then by a decay due to evaporation as the ambient air gets drier and the aerosol plume is diluted. Coagulation and evaporation are obviously not exclusive and their competition depends on the ambient conditions that vary over space and time (Hamill et al., 1977). It is also apparent from Fig. 1 that the moist layer is less confined than the aerosol layer and extends in latitude beyond the limits of the figure. The extinction-to-backscatter ratio is also smaller on the periphery of the aerosol plume (Fig. 2~~e~~g). Therefore, we expect evaporation of the transported sulphate aerosols to occur at such latitudes.

The similarity of the extinction-to-backscatter ~~in those~~ (Fig. 2g) in the two latitude slices 25°S-15°S and 15°S-5°S implies common microphysical properties. However, the curves of extinction and backscatter~~taken separately are very different from mid-February to mid-May as can be~~, taken separately, evolve differently as inferred from Fig. 2a&c.

3 ~~Composition~~ Inferred composition of the plume

We now consider the history of the aerosol composition of the plume. The sequence in Fig. 3a-d shows, in agreement with Carr et al. (2022), S2022 and Khaykin et al. (2022), that the ash and ice ~~plume~~ cloud (brown and deep blue) is rapidly ~~washed down~~ removed within the first day following the eruption likely via sedimentation within large ice particles. Taha et al. (2022) mention that ashes are missing in the plume on 17 January from UV satellite observations. What emerges on the west side are two greenish clouds (Fig. 3d) without any hint of ash (~~that~~ ashes would appear as yellow/reddish). The early CALIOP ~~section~~ cross section through these clouds (Fig. 3e-f) shows ~~the two aerosol clouds as~~ high-scattering-ratio ~~patches~~ without depolarization, hence ~~made of~~ indicative of predominantly small spherical particles. A few days later, the ~~LOAC~~ Light Optical Aerosol Counter flight from La Réunion brings confirmation by showing ~~sub-micronic~~sub-micron size, mainly non-absorbing, particles (Kloss et al., 2022).

A further source of information is from the Infrared/Microwave Sounder (IMS) retrieval (Appendix A1.2) of SO_2 column and Sulphate Aerosols Optical Depth (SA/OD). Figure 3g-h shows that the conversion to sulphates started immediately after the eruption with an SA/OD reaching 0.1 one day after the eruption suggesting the two clouds seen by CALIOP are composed of almost pure sulphate droplets. The fast conversion of SO_2 to sulphate ~~aeerosols~~ aerosols is also discussed by S2022 and Zhu et al. (2022), using observations and chemical/transport modelling, respectively.

Four days later (Fig. 4b), the two ~~components of the plume~~ clouds are still separated but have elongated under the zonal shear forming a pair of long strips. Comparing Figs. 4a and b, makes apparent that the conversion to sulphates is almost complete in the western strip associated to the western and highest cloud ~~(~~in Fig. 3e ~~)~~ while it is incomplete in the eastern strip associated to the eastern ~~cloud~~and lowest cloud in Fig. 3e. S2022 show that the western cloud is much moister than the eastern one, offering a likely reason for faster conversion, as also discussed by Zhu et al. (2022). A cloud of almost pure SO_2 is located between Australia and Indonesia (Fig. 4a), at lower altitudes than the other two clouds (as inferred from its low angular speed). Comparing the IMS products to RGB-Ash (Fig. 4c) demonstrates that RGB-Ash shows sulphates rather than SO_2 as usually assumed. The sensitivity of geostationary broad-band products, like RGB-Ash, to sulphates is shown by Sellitto and Legras (2016).

The conversion of remaining SO_2 to sulphates proceeds until SO_2 returns to background conditions by late January (Fig. 4d). The sulphates persist for ~~several months~~ at least six months (Fig. 1) and the comparison of Fig. 4e and f shows that zonal averages of IMS and CALIOP products exhibit very similar patterns. The CALIOP depolarization never exceeds its initial value (Fig. 3f) until ~~June~~July.

4 Circumnavigation and instabilities

Figure 5 shows the circumnavigation of the sulphate ~~plumes~~ plume from a series of IMS SA/OD maps over one month and half ~~. The supplement movie (B) provides~~ ~~(~~an extended view until 30 April is provided by the supplement movie (Appendix B)). Due to the differential rotation, the fastest patches near 5°S caught the slowest by 30°S by mid-February and the plume filled the whole latitude circle. As time proceeds the components of the plume kept elongating and mixed together towards a zonal uniformity (see movie).

However, Figure 5 shows a number of localized concentrated patches which persist and keep forming in the plume one month after the eruption. Figure 6 investigates the structure of some of them and compares the IMS SA/OD to the observations from active instruments. Figure 6a shows an early case during the blackout period of CALIOP on 24 January. Using the Atmospheric Laser Doppler Instrument (ALADIN) (Appendix A1.5), Figure 6b shows that an anticyclonic anomalous shear spans the highest patch (28 km) which is part of the western strip defined in previous section. The same pattern is observed on 28 January (Fig. 6c) across a patch near 11°E and 25°S (Fig. 5a) which belongs to the eastern strip. A CALIOP section is available (Fig. 6d) which exhibits a "jelly fish" pattern with a head at 26 km connected by a tail to lower altitude patches along an arc of same angular speed (Fig. A1a). This pattern is found repetitively on ~~CALIOP sections and corresponds to the quasi-circular patches often seen in the SA/OD and RGB-Ash maps~~subsequent CALIOP sections (not shown).

On 30 January 2022, we are back on the western strip (Fig. 6e) and the CALIOP section (Fig. 6f) shows a hairy pattern above the main patch that we interpret as the tail left by the fast descent. Again this pattern is repetitively observed on CALIOP sections across the western strip until mid-February where the fast descent halts.

A remarkable feature in SA/OD maps are the trains of compact elliptical ~~structure~~ structures linked together by filaments which are visible all along February and early March in Fig. 5 and the supplement movie. This peculiar shape is reminiscent of shear-induced instabilities ~~as documented, e.g., by Juckes (1995), which lead~~ (Juckes, 1995), leading to the formation of a chain of ~~quasi-circular~~ vortices. The suspicion is reinforced by the pattern of a wrapping up tripolar structure seen near 180°E on 11 February (Fig. 6g) and perfectly captured by CALIOP as a core surrounded by two arms at the same level (Fig. 6h). This comparison also reveals the amount of relevant small-scale details retrieved by the IMS product.

Barotropic shear instability requires a reversal of the meridional gradient of absolute vorticity. The mean flow in ERA5 does not satisfy this criterion. A generalized baroclinic instability requires a reversal of the potential vorticity gradient but the mean flow again hardly satisfies this criterion at the required altitude of 25 km (Fig. A2). The very fact that the instability produces aerosol patches suggests they are related to the generation of vorticity. The detection of an anomalous anticyclonic shear across the concentrated patches of the plume by ALADIN supports this hypothesis. However, sulphates are poor absorbers and neither these vortical structures nor their thermal signature have been detected by our present investigation of the ERA5. Therefore, this observation still requires an explanation that we leave for future studies.

5 Discussion and conclusion

The very intense and unusual ~~Hunga Tonga~~ HTHH eruption generated an intense and unusual stratospheric plume with a huge amount of injected water vapour that remains well above normal 6 months after the eruption. After a fast initial removal of ice and ashes, the bulk of the remaining plume consisted of two main clouds between 26 and 32 km traveling westward due to the prevailing phase of the QBO. The ensuing zonal transport dispersed the plume ~~all around the Earth within a few weeks~~ through all longitudes in less than a month (see also Khaykin et al., 2022). The initial SO_2 is fully converted into sulphates in less than two weeks under the influence of water vapour.

The fast initial descent of the upper part of the plume induced by the radiative water vapour cooling has concentrated the aerosols within a fairly narrow layer, about 2 km thick as shown from CALIOP measurements (Figs. 1&3). Within the limit of MLS resolution, the water vapour then coincides with the aerosols. The aerosols later continued subsiding at a slower rate under the effect of gravitational sedimentation, whereas the moist layer entrained by the Brewer-Dobson circulation was simultaneously ascending, so that the two layers progressively decoupled (as also seen by Schoeberl et al., 2022). Although a precise sequencing is difficult without quantitative modelling, it is likely that the sulphate aerosols first grew by hydration, then by coagulation and ended by dwindling under evaporation. Our estimation of fall speed and extinction-to-backscatter ratio trends is consistent with a growth up to about 1.5 ~~-2.0~~ µm and then a decrease in mean size.

The ~~data show a~~ fast conversion of SO_2 ~~to sulphates enhanced by water vapour and therefore~~ suggests that the initial sulphur injection might have been ~~strongly~~ underestimated. Consistently, S2022 showed that the ~~Hunga Tonga~~ HTHH eruption produced the largest stratospheric aerosol perturbation since the Pinatubo eruption in 1991, and suggested a large potential for climatic impacts (see also Khaykin et al., 2022). By June, the hemispheric stratospheric aerosol optical depth perturbation of the ~~Hunga Tonga~~ HTHH plume is twice as large as the peak perturbation of the 2019 Raikoke eruption, and the tropical impact is at least three times as large as any volcanic perturbation since Pinatubo 1991 ~~(OMPS-LP data, not shown here)~~(S2022, Khaykin et al., 2022). As the SO_2 emissions for the Raikoke eruption have been estimated at 1.5 Tg (de Leeuw et al., 2021), we assume this value as the lower limit for the ~~Hunga Tonga~~ HTHH eruption, three times larger than early estimates (Witze, 2022). The young aerosols seem mostly made of sub-micronic liquid sulphate particles then growing to ~~1-2~~1.5 $\mu\mathrm{m}$ due to hydration/coagulation/evaporation. The dispersion of the plume questions the magnitude and the duration of the impact. An early estimate of the ~~plume~~ resulting radiative forcing by S2022 shows that stratospheric aerosol and water vapour perturbations from the eruption may significantly impact the climate system. Given the large greenhouse potential of stratospheric water vapour ~~(Solomon et al., 2010)~~(e.g. Solomon et al., 2010), it was proposed that the dispersed plume has a net warming effect (S2022), in contrast with the cooling expected from stratospheric aerosols.

Finally, we have shown that the ~~plume~~ dynamics repetitively generates compact aerosol ~~circular~~ structures in a process that bears similarities with shear instability.

Appendix A: Data and methods

A1 Observations

We use data from the following instruments and products.

A1.1 CALIOP

The Cloud-Aerosol Lidar with Orthogonal Polarisation (CALIOP) is a spaceborne lidar onboard the CALIPSO satellite (Vaughan et al., 2004; Winker et al., 2010). We use the L1 532 nm attenuated backscatter which is filtered in the horizontal with a median filter of width ~~101~~ 102 km. In particular, this filter removes the noise associated with the South Atlantic Anomaly (SAA) which perturbs CALIOP data between 30°W and 80°W (Noel et al., 2014). In practice, a limited amount of data are usable in this region and only at night. After filtering, the data are further averaged at a resolution of 34 km for compactness. The other channels are processed in the same way.

Due to solar activity, CALIOP was not operating on 18 January and between 20 and 26 January. Hence, our CALIOP series start on 27 January. We use only night data in this work. The molecular backscatter is calculated following Hostetler et al. (2006). For each day, the backscatter ratio is zonally averaged other all available orbits of that day (14 to 15 for a nominal day). The native vertical resolution in the 20-30 km range is 180 m.

A1.2 IMS

The RAL (Rutherford Appleton Laboratory) Infrared/Microwave Sounder (IMS) retrieval core scheme (Siddans, 2019) uses an optimal estimation spectral fitting procedure to retrieve atmospheric and surface parameters jointly from co-located measurements by IASI (Infrared Atmospheric Sounding Interferometer), AMSU (Advanced Microwave Sounding Unit) and MHS (Microwave Humidity Sounder) on MetOp-B spacecraft, using RTTOV 12 (Radiative Transfer for TOVS)(Saunders et al., 2017) as the forward radiative transfer model. The use of RTTOV 12 enables the quantitative retrieval of volcanic-specific aerosols (sulphate aerosol) and trace gases (SO_2). The present paper uses IMS SO_2 and sulphate aerosols observations from its near-real time implementation. The IMS scheme retrieves the SO_2 in the sensitive region around 1100-1200 cm^{-1}, in ppbv assuming a uniform vertical mixing ratio. It retrieves sulphate-specific ~~AOD (Aerosol Optical Depth) at 1200~~optical depth at 1170 cm^{-1} (i.e. the peak of the mid-infrared extinction cross section (Sellitto and Legras, 2016)), assuming a Gaussian extinction coefficient profile shape peaking at 20 km altitude, with 2 km full-width half-maximum. The bulk of the spectroscopic information on SO_2 and sulphate aerosols, in the IMS scheme, thus comes from the IASI Fourier transform spectrometer (Clerbaux et al., 2009). We refer to the two retrieved product as IMS SO_2 and IMS SA/OD in this work. The data are provided daily on a regular grid with 0.25°resolution in latitude and longitude with one image collecting the day swaths and another collecting the night swaths.

A1.3 OMPS-LP

The Ozone Mapping and Profiler Suite Limb Profiler (OMPS-LP) onboard the Suomi-NPP satellite provides along track vertical profiles of aerosol extinction in several visible bands (Loughman et al., 2018; Taha and Loughman, 2020). We use version 2.1 and the 745 nm band as recommended by Taha et al. (2021). Swaths with non zero quality flag are discarded. Basically, this filters data polluted by the SAA but filtered and non filtered results differ very little in our processing. The molecular extinction is calculated from the same formulas as the CALIOP molecular backscatter but for a change of wavelength. The extinction is averaged daily over all available orbits of that day and after a horizontal interpolation to a latitude grid of 1.1°resolution that corresponds to the mean resolution of OMPS-LP in the considered range of latitudes. The native vertical resolution is 1 km.

A1.4 MLS

The Microwave Limb Sounder (MLS) onboard NASA's AURA satellite provides along track vertical profiles of water vapour mixing ratio ~~(Lambert et al., 2015)~~(Lambert et al., 2015; Schwartz et al., 2020). We use the version 4 without accounting the quality flag as in Millán et al. (2022). The data are projected and zonally averaged daily onto a fixed latitude grid of 1.45°resolution in the domain of interest. As they are provided on pressure levels they are interpolated to altitudes using the geopotential calculated daily on the ERA5 zonal mean. In order to get estimates of the altitudes by the method described in Appendix A3, the interpolation is made to a resolution of 100 m using a non-oscillating Akima interpolator.

A1.5 ALADIN

The Atmospheric Laser Doppler Instrument (ALADIN) onboard the Aeolus satellite is the first space-borne Doppler wind lidar. It is designed to measure wind along the line of sight from the Doppler shift of the 355 nm light emitted by the laser and scattered back by molecules (Rayleigh wind) or aerosols (Mie wind). Horizontal line-of-sight wind is retrieved neglecting the vertical wind component. The anomaly wind is calculated by removing the background wind at same time and location from ERA5. As the line-of-sight is perpendicular to the heliosynchronous orbit, the measured component at low and mid-latitudes is essentially the zonal wind. The ceiling of Aeolus vertical bins can be adjusted and was increased to 30 km in the area of the ~~Hunga Tonga~~ HTHH plume ($30°$S-$0°$) a few days after the eruption. At high altitude, the Mie product is of better quality inside the plume and is used in the present study.

A1.6 RGB-Ash

We use a composite RGB product, denoted as RGB-Ash, that benefits from the sensitivity of the 8.5 $\mu\mathrm{m}$ band of the Advanced Himawari Imager (AHI) and Spanning Enhanced Visible and InfraRed Imager (SEVIRI) onboard the geostationary Himawari-8 and Meteosat-8 satellites. The product is based on the EUMETSAT Ash RGB recipe (https://navigator.eumetsat.int/product/EO:EUM:DAT:MSG:VOLCANO/print) and uses the brightness temperatures (BT in K) of the three channels: 8.5, 10.4 and 12.3 $\mu\mathrm{m}$. The recipe for the three colour indexes ranging from 0 to 1 is $R = (\mathrm{BT}(12.3) - \mathrm{BT}(10.4) + 2574)/6$, $G = (\mathrm{BT}(10.4) - \mathrm{BT}(8.5) + 4)/9$ and $B = (\mathrm{BT}(10.4) - 243)/60$. The same recipe is used for both instruments even if the channels are not strictly identical. This product allows to qualitatively distinguish thick ash plumes or ice clouds (brown), thin ice clouds (dark blue) and sulphur-containing plumes (green). Mixed ash/sulphur-containing volcanic species would appear in reddish and yellow shades.

A2 ERA5 reanalysis and meteorological data

We use the European Center for Medium Range Forecasts ERA5 reanalysis (Hersbach et al., 2020) at $1° \times 1°$resolution and the model levels with 6-hourly sampling ~~. The data are averaged daily~~ at 0, 6, 12 and ~~zonally.~~ 18 UTC. Geopotential, potential temperature and potential vorticity are calculated at full resolution for each time. All the fields are then averaged in longitude and other the four daily samples to provide a daily zonal average. At the stratospheric altitudes which are relevant to this study, the model levels are pure pressure and therefore the averages are made over isobars.

The total all sky radiative heating rate is converted into diabatic vertical velocity from the relation between geopotential and potential temperature. The motion of the potential temperature lines with respect to the geopotential in the zonal mean is used to define the adiabatic vertical velocity. The ERA5 does not assimilate the anomalous water vapour or the aerosols in the stratosphere and therefore cannot account for their direct radiative effect. It can only assimilate the induced local temperature perturbation if large enough and then react to damp it (Lestrelin et al., 2021). In the present case, the temperature assimilation is further perturbed by the effect of water vapour on the GPS or the infrared signals, provided the assimilation system does not reject the data.

The Lait potential vorticity (LPV) used in Fig.A2 is defined from the Ertel potential vorticity (PV) as

$$\mathrm{LPV} = \left(\frac{600}{\theta}\right)^4 \mathrm{PV},$$

where θ is the potential temperature in K.

A3 Vertical motion from CALIOP and MLS

The observed vertical motion is obtained from CALIOP and MLS by applying a second-order Savitsky-Golay filter with a ~~21-day~~ 31-day window to the daily mean vertical location of CALIOP scattering ratio and MLS water vapour, retaining data above 2 and 6 ppmv offsets, respectively. The offset are defined to isolate the aerosol and the water plumes from the background. The 31-day window has been adjusted from several trials with 11, 21, 31 and 41 days as the value beyond which the resulting motion curve was rid of short time fluctuations and did not change any more in shape. This was reached with 31-day for MLS and 21-day for CALIOP but in the sake of consistency we use 31-day for both.

In order to compensate for background air motion and the motion of isentropic surfaces with respect to geopotential surfaces, the diabatic and adiabatic background vertical velocity are calculated from ERA5. The diabatic motion results from the total radiative heating rate $\frac{DT}{Dt}|_{\mathrm{RAD}}$ multiplied by $\frac{\theta}{T}\frac{\delta z}{\delta\theta}$ where (T,θ,z) are temperature, potential temperature and geopotential altitude. The adiabatic motion, which is always a small correction, is estimated as $-\frac{\partial\theta}{\partial t}|_p\frac{\delta z}{\delta\theta} + \frac{\partial z}{\partial t}|_p$. The calculations are made by centered finite differences on the model grid which is in pure pressure in the considered latitude range. A resulting corrected aerosol motion with respect to the ERA5 air is then calculated by removing the diabatic and adiabatic motions from the observed vertical motion.

A4 Mie calculations

The theoretical extinction-to-backscatter ratio for the plume has been calculated using the Python-based miepython Mie code, available at: https://miepython.readthedocs.io/en/latest/. The extinction and backscatter coefficients have been estimated at 750 and 532 nm, respectively, to simulate OMPS and CALIOP observations. Typical sulphate aerosols refractive indices have been considered, with the assumption of very weakly absorbing particles (based on the results of (Kloss et al., 2022)). Log-normal size distributions with varying standard deviation are simulated, to study how this ratio changes with radius.

Appendix B: IMS animation

The animation https://mycore.core-cloud.net/index.php/s/CQdtD1VLY2xYuKe shows the IMS SA/OD product for all day and night orbits of each day between 13 January and 30 April 2022. The indicated times are those of the intersection of the orbits with the equator. When two orbit swaths overlap, the crossing time of the overlapped orbit is indicated in red. Missing orbits are blanked out. Several days are entirely missing between 8 and 14 March.

Code and data availability. MLS and OMPS-LP data are available from EarthData centre at: https://disc.gsfc.nasa.gov/. CALIOP data v3.41 are available at: https://doi.org/10.5067/CALIOP/CALIPSO/CAL_LID_L1-VALSTAGE1-V3-41. ALADIN data are available from ESA at https://earth.esa.int/eogateway/missions/aeolus/data. IMS data will be available on a public deposit. ERA5 data are available at https://www.ecmwf.int/en/forecasts/datasets/reanalysis-datasets/era5. The python scripts and notebooks used in this study will be available at https://github.com/bernard-legras/ASTuS under tag v2.2

Video supplement. https://mycore.core-cloud.net/index.php/s/CQdtD1VLY2xYuKe

Author contributions. BL, PS and AP conceived the study and conducted the analyses. EC and RS elaborated and provided the IMS product. JUG, SK and FP were involved in discussions of the results and their interpretation. The paper was written by BL, CD, PS and AP. All authors contributed to the final version.

Competing interests. The authors declare no competing interests.

Acknowledgements. The CALIOP and GEOs data have been provided by the AERIS/ICARE Data and Service Centre and processed using the centre computer resoources. ERA5 data were provided by Copernicus Climate Change Service. We acknowledge support from the Agence Nationale de la Recherche under grants 21-CE01-0007-01 (ASTuS), 21-CE01-0028-01 (TuRTLES) and 21-CE01-0028-01 (PyroStrat). We acknowledge discussions with Paul Billant, Guillaume Carazzo, Corinna Kloss, Guillaume Lapeyre, Angela Limare and Tjarda Roberts.

References

Carr, J. L., Horvath, A., Wu, D. L., and Friberg, M. D.: Stereo Plume Height and Motion Retrievals for the Record-Setting Hunga Tonga-Hunga Ha'apai Eruption of 15 January 2022, Geophysical Research Letters, https://doi.org/10.1029/2022GL098131, 2022.

Clerbaux, C., Boynard, A., Clarisse, L., George, M., Hadji-Lazaro, J., Herbin, H., Hurtmans, D., Pommier, M., Razavi, A., Turquety, S., Wespes, C., and Coheur, P.-F.: Monitoring of atmospheric composition using the thermal infrared IASI/MetOp sounder, Atmospheric Chemistry and Physics, 9, 6041–6054, https://doi.org/10.5194/acp-9-6041-2009, 2009.

de Leeuw, J., Schmidt, A., Witham, C. S., Theys, N., Taylor, I. A., Grainger, R. G., Pope, R. J., Haywood, J., Osborne, M., and Kristiansen, N. I.: The 2019 Raikoke volcanic eruption – Part 1: Dispersion model simulations and satellite retrievals of volcanic sulfur dioxide, Atmospheric Chemistry and Physics, 21, 10 851–10 879, https://doi.org/10.5194/acp-21-10851-2021, 2021.

Gorkavyi, N., Krotkov, N., Li, C., Lait, L., Colarco, P., Carn, S., DeLand, M., Newman, P., Schoeberl, M., Taha, G., Torres, O., Vasilkov, A., and Joiner, J.: Tracking aerosols and SO2 clouds from the Raikoke eruption: 3D view from satellite observations, Atmospheric Measurement Techniques, 14, 7545–7563, https://doi.org/10.5194/amt-14-7545-2021, 2021.

Hamill, P., Toon, O. B., and Kiang, C. S.: Microphysical Processes Affecting Stratospheric Aerosol Particles, Journal of the Atmospheric Sciences, 34, 1104–1119, https://doi.org/10.1175/1520-0469(1977)034<1104:MPASAP>2.0.CO;2, 1977.

Hersbach, H., Bell, B., Berrisford, P., Hirahara, S., Horányi, A., Muñoz-Sabater, J., Nicolas, J., Peubey, C., Radu, R., Schepers, D., Simmons, A., Soci, C., Abdalla, S., Abellan, X., Balsamo, G., Bechtold, P., Biavati, G., Bidlot, J., Bonavita, M., Chiara, G., Dahlgren, P., Dee, D., Diamantakis, M., Dragani, R., Flemming, J., Forbes, R., Fuentes, M., Geer, A., Haimberger, L., Healy, S., Hogan, R. J., Hólm, E., Janisková, M., Keeley, S., Laloyaux, P., Lopez, P., Lupu, C., Radnoti, G., Rosnay, P., Rozum, I., Vamborg, F., Villaume, S., and Thépaut, J.: The ERA5 global reanalysis, Quarterly Journal of the Royal Meteorological Society, 146, 1999–2049, https://doi.org/10.1002/qj.3803, 2020.

Hostetler, C. A., Liu, Z., Reagan, J. A., Vaughan, M., Winker, D., Osborn, M., Hunt, W. H., Powell, K. A., and Trepte, C.: CALIOP Algorithm Theoretical Basis Document. Calibration and Level 1 Data Products, Tech. Rep. Doc. PS-SCI-201, NASA Langley Res. Cent., Hampton, VA, https://www-calipso.larc.nasa.gov/resources/pdfs/PC-SCI-201v1.0.pdf, 2006.

Juckes, M.: Instability of surface and upper-tropospheric shear lines, J. Atmos. Sci., 52, 3247–3262, 1995.

Khaykin, S., Podglajen, A., Ploeger, F., Grooß, J.-U., Tence, F., Bekki, S., Khlopenkov, K., Bedka, K., Rieger, L., Baron, A., Godin-Beekmann, S., Legras, B., Sellitto, P., Sakai, T., Barnes, J., Uchino, O., Morino, I., Nagai, T., Wing, R., Baumgarten, G., Gerding, M., Duflot, V., Payen, G., Jumelet, J., Querel, R., Liley, B., Bourassa, A., Hauchecorne, A., Ravetta, F., Clouser, B., and Feofilov, A.: Global perturbation of stratospheric water and aerosol burden by Hunga eruption, https://doi.org/10.1002/essoar.10511923.1, 2022.

Kloss, C., Sellitto, P., Renard, J., Baron, A., Bègue, N., Legras, B., Berthet, G., Briaud, E., Carboni, E., Duchamp, C., Duflot, V., Jacquet, P., Marquestaut, N., Metzger, J., Payen, G., Ranaivombola, M., Roberts, T., Siddans, R., and Jégou, F.: Aerosol Characterization of the Stratospheric Plume From the Volcanic Eruption at Hunga Tonga 15 January 2022, Geophysical Research Letters, 49, https://doi.org/10.1029/2022GL099394, 2022.

Lambert, A., Livesey, N. J., and Read, W.: MLS/Aura L2 Water Vapor (H2O) Mixing Ratio - Version 4, https://doi.org/10.5067/AURA/MLS/DATA2009, 2015.

Lestrelin, H., Legras, B., Podglajen, A., and Salihoglu, M.: Smoke-charged vortices in the stratosphere generated by wildfires and their behaviour in both hemispheres: comparing Australia 2020 to Canada 2017, Atmospheric Chemistry and Physics, 21, 7113–7134, https://doi.org/10.5194/acp-21-7113-2021, 2021.

Loughman, R., Bhartia, P. K., Chen, Z., Xu, P., Nyaku, E., and Taha, G.: The Ozone Mapping and Profiler Suite (OMPS) Limb Profiler (LP) Version 1 aerosol extinction retrieval algorithm: theoretical basis, Atmospheric Measurement Techniques, 11, 2633–2651, https://doi.org/10.5194/amt-11-2633-2018, 2018.

Matoza, R. S., Fee, D., Assink, J. D., Iezzi, A. M., Green, D. N., Kim, K., Toney, L., Lecocq, T., Krishnamoorthy, S., Lalande, J.-M., Nishida, K., Gee, K. L., Haney, M. M., Ortiz, H. D., Brissaud, Q., Martire, L., Rolland, L., Vergados, P., Nippress, A., Park, J., Shani-Kadmiel, S., Witsil, A., Arrowsmith, S., Caudron, C., Watada, S., Perttu, A. B., Taisne, B., Mialle, P., Le Pichon, A., Vergoz, J., Hupe, P., Blom, P. S., Waxler, R., De Angelis, S., Snively, J. B., Ringler, A. T., Anthony, R. E., Jolly, A. D., Kilgour, G., Averbuch, G., Ripepe, M., Ichihara, M., Arciniega-Ceballos, A., Astafyeva, E., Ceranna, L., Cevuard, S., Che, I.-Y., De Negri, R., Ebeling, C. W., Evers, L. G., Franco-Marin, L. E., Gabrielson, T. B., Hafner, K., Harrison, R. G., Komjathy, A., Lacanna, G., Lyons, J., Macpherson, K. A., Marchetti, E., McKee, K. F., Mellors, R. J., Mendo-Pérez, G., Mikesell, T. D., Munaibari, E., Oyola-Merced, M., Park, I., Pilger, C., Ramos, C., Ruiz, M. C., Sabatini, R., Schwaiger, H. F., Tailpied, D., Talmadge, C., Vidot, J., Webster, J., and Wilson, D. C.: Atmospheric waves and global seismoacoustic observations of the January 2022 Hunga eruption, Tonga, Science, https://doi.org/10.1126/science.abo7063, 2022.

Millán, L., Santee, M. L., Lambert, A., Livesey, N. J., Werner, F., Schwartz, M. J., Pumphrey, H. C., Manney, G. L., Wang, Y., Su, H., Wu, L., Read, W. G., and Froidevaux, L.: The Hunga Tonga-Hunga Ha'apai Hydration of the Stratosphere, Geophysical Research Letters, 49, e2022GL099 381, https://doi.org/10.1029/2022GL099381, 2022.

Noel, V., Chepfer, H., Hoareau, C., Reverdy, M., and Cesana, G.: Effects of solar activity on noise in CALIOP profiles above the South Atlantic Anomaly, Atmospheric Measurement Techniques, 7, 1597–1603, https://doi.org/10.5194/amt-7-1597-2014, 2014.

Podglajen, A., Le Pichon, A., Garcia, R. F., Gerier, S., Millet, C., Bedka, K. M., Khlopenkov, K. V., Khaykin, S. M., and Hertzog, A.: Balloon-borne observations of acoustic-gravity waves from the 2022 Hunga Tonga eruption in the stratosphere, submitted to Earth and Space Science, https://doi.org/10.1002/essoar.10511570.1, 2022.

Poli, P. and Shapiro, N. M.: Rapid Characterization of Large Volcanic Eruptions: Measuring the Impulse of the Hunga Tonga Ha'apai Explosion From Teleseismic Waves, Geophysical Research Letters, 49, https://doi.org/10.1029/2022GL098123, 2022.

Proud, S. R., Prata, A., and Schmauss, S.: The January 2022 eruption of Hunga Tonga-Hunga Ha'apai volcano reached the mesosphere, https://doi.org/10.1002/essoar.10511092.1, 2022.

Saunders, R., Hocking, J., Rundle, D., Rayer, P., Hayemann, S., Matricardi, A., Lupu, C., Brunel, P., and Vidot, J.: RTTOV-12 SCIENCE AND VALIDATION REPORT; Version : 1.0, Doc ID : NWPSAF-MO-TV-41, https://nwp-saf.eumetsat.int/site/download/documentation/rtm/docs_rttov12/rttov12_svr.pdf, 2017.

Schoeberl, M., Ueyama, R., Taha, G., Jensen, E., and Yu, W.: Analysis and impact of the Hunga Tonga-Hunga Ha'apai Stratospheric Water Vapor Plume, https://doi.org/10.1002/essoar.10511762.1, 2022.

Schwartz, M. J., Santee, M. L., Pumphrey, H. C., Manney, G. L., Lambert, A., Livesey, N. J., Millán, L., Neu, J. L., Read, W. G., and Werner, F.: Australian New Year's PyroCb Impact on Stratospheric Composition, Geophysical Research Letters, https://doi.org/10.1029/2020GL090831, 2020.

Seinfeld, J. H. and Pandis, S. N.: Atmospheric chemistry and physics: from air pollution to climate change, John Wiley & Sons, ISBN:978-1-119-22116-6 978-1-119-22117-3 Third edition,, 2016.

Sellitto, P. and Legras, B.: Sensitivity of thermal infrared nadir instruments to the chemical and microphysical properties of UTLS secondary sulfate aerosols, Atmospheric Measurement Techniques, 9, 115–132, https://doi.org/10.5194/amt-9-115-2016, 2016.

Sellitto, P., Podglajen, A., Belhadji, R., Boichu, M., Carboni, E., Cuesta, J., Duchamp, C., Kloss, C., Siddans, R., Begue, N., Blarel, L., Jegou, F., Khaykin, S., Renard, J.-B., and Legras, B.: The unexpected radiative impact of the Hunga Tonga eruption of January 15th, 2022, preprint, in review, https://doi.org/10.21203/rs.3.rs-1562573/v1, 2022.

Siddans, R.: Water Vapour Climate Change Initiative (WV-CCI) - Phase One, Deliverable 2.2; Version 1.0, Tech. Rep. D2.2, STFC Rutherford Appleton Laboratory (RAL), https://climate.esa.int/documents/1337/Water_Vapour_CCI_D2.2_ATBD_Part2-IMS_L2_product_v1.0.pdf, 2019.

Solomon, S., Rosenlof, K. H., Portmann, R. W., Daniel, J. S., Davis, S. M., Sanford, T. J., and Plattner, G.-K.: Contributions of stratospheric water vapor to decadal changes in the rate of global warming., Science, 327, 1219–1223, https://doi.org/10.1126/science.1182488, 2010.

Taha, G. and Loughman, R.: OMPS-NPP L2 LP Aerosol Extinction Vertical Profile swath daily 3slit V2, https://doi.org/10.5067/CX2B9NW6FI27, 2020.

Taha, G., Loughman, R., Zhu, T., Thomason, L., Kar, J., Rieger, L., and Bourassa, A.: OMPS LP Version 2.0 multi-wavelength aerosol extinction coefficient retrieval algorithm, Atmospheric Measurement Techniques, 14, 1015–1036, https://doi.org/10.5194/amt-14-1015-2021, 2021.

Taha, G., Loughman, R., Colarco, P. R., Zhu, T., Thomason, L. W., and Jaross, G.: Tracking the 2022 Hunga Tonga-Hunga Ha'apai aerosol cloud in the upper and middle stratosphere using space-based observations, 2022.

Vaughan, M. A., Young, S. A., Winker, D. M., Powell, K. A., Omar, A. H., Liu, Z., Hu, Y., and Hostetler, C. A.: Fully automated analysis of space-based lidar data: an overview of the CALIPSO retrieval algorithms and data products, Proc. SPIE 5575, Laser Radar Techniques for Atmospheric Sensing, (4 November 2004), https://doi.org/10.1117/12.572024, 2004.

Vergoz, J., Hupe, P., Listowski, C., Le Pichon, A., Garcés, M., Marchetti, E., Labazuy, P., Ceranna, L., Pilger, C., Gaebler, P., Näsholm, S., Brissaud, Q., Poli, P., Shapiro, N., De Negri, R., and Mialle, P.: IMS observations of infrasound and acoustic-gravity waves produced by the January 2022 volcanic eruption of Hunga, Tonga: A global analysis, Earth and Planetary Science Letters, 591, 117 639, https://doi.org/10.1016/j.epsl.2022.117639, 2022.

Winker, D. M., Pelon, J., Coakley, J. A., Ackerman, S. A., Charlson, R. J., Colarco, P. R., Flamant, P., Fu, Q., Hoff, R. M., Kittaka, C., Kubar, T. L., Le Treut, H., Mccormick, M. P., Mégie, G., Poole, L., Powell, K., Trepte, C., Vaughan, M. A., and Wielicki, B. A.: The CALIPSO Mission: A Global 3D View of Aerosols and Clouds, Bulletin of the American Meteorological Society, 91, 1211–1230, https://doi.org/10.1175/2010BAMS3009.1, 2010.

Witze, A.: Why the Tongan eruption will go down in the history of volcanology, Nature, 602, 376–378, https://doi.org/10.1038/d41586-022-00394-y, 2022.

Wright, C. J., Hindley, N. P., Alexander, M. J., Barlow, M., Hoffmann, L., Mitchell, C. N., Prata, F., Bouillon, M., Carstens, J., Clerbaux, C., Osprey, S. M., Powell, N., Randall, C. E., and Yue, J.: Surface-to-space atmospheric waves from Hunga Tonga-Hunga Ha'apai eruption, Nature, https://doi.org/10.1038/s41586-022-05012-5, 2022.

Zhang, H., Wang, F., Li, J., Duan, Y., Zhu, C., and He, J.: Potential Impact of Tonga Volcano Eruption on Global Mean Surface Air Temperature, Journal of Meteorological Research, 36, 1–5, https://doi.org/10.1007/s13351-022-2013-6, 2022.

Zhu, Y., Bardeen, C., Tilmes, S., Mills, M., Harvey, V., Taha, G., Kinnison, D., Yu, P., Rosenlof, K., Wang, X., Avery, M., Kloss, C., Li, C., Glanville, A., Millan, L., Deshler, T., Portmann, R., Krotkov, N., and Toon, O.: 2022 Hunga-Tonga eruption: stratospheric aerosol evolution in a water-rich plume, preprint, in review, https://doi.org/10.21203/rs.3.rs-1647643/v1, 2022.

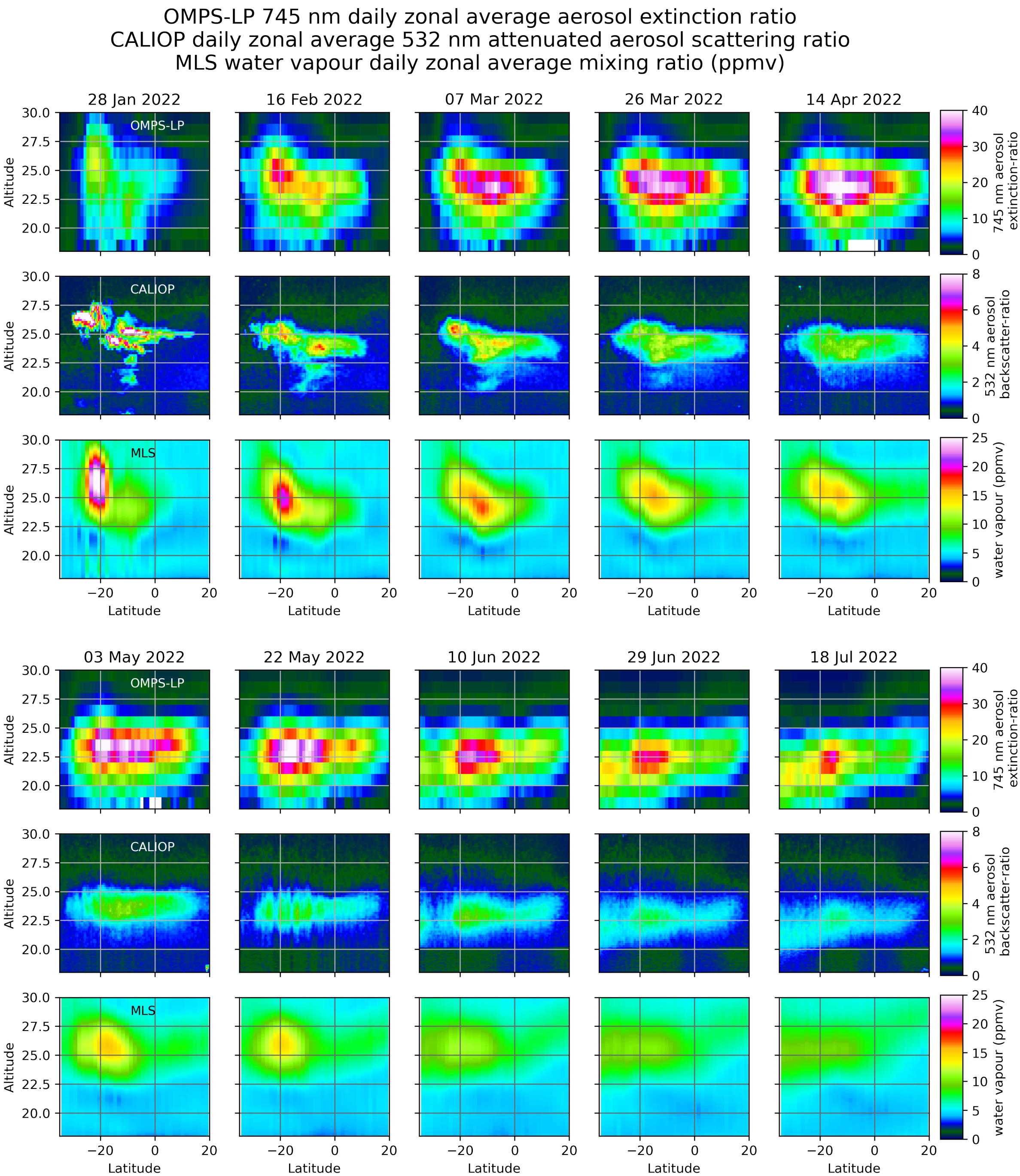

Figure 1. Series of daily zonal averages over all available orbits from three satellites measuring aerosols and water vapour (Appendices A1.3, A1.1 and A1.4). The series is shown in two consecutive blocks of three rows. Upper row: OMPS-LP 745 nm aerosol extinction ratio. Middle row: CALIOP 532 nm aerosol attenuated backscatter ratio. Lower row: MLS water vapour (in ppmv). Days from 28 ~~/01/~~January 2022 to ~~04/06/~~16 July 2022 with ~~16-day~~ 19-day step.

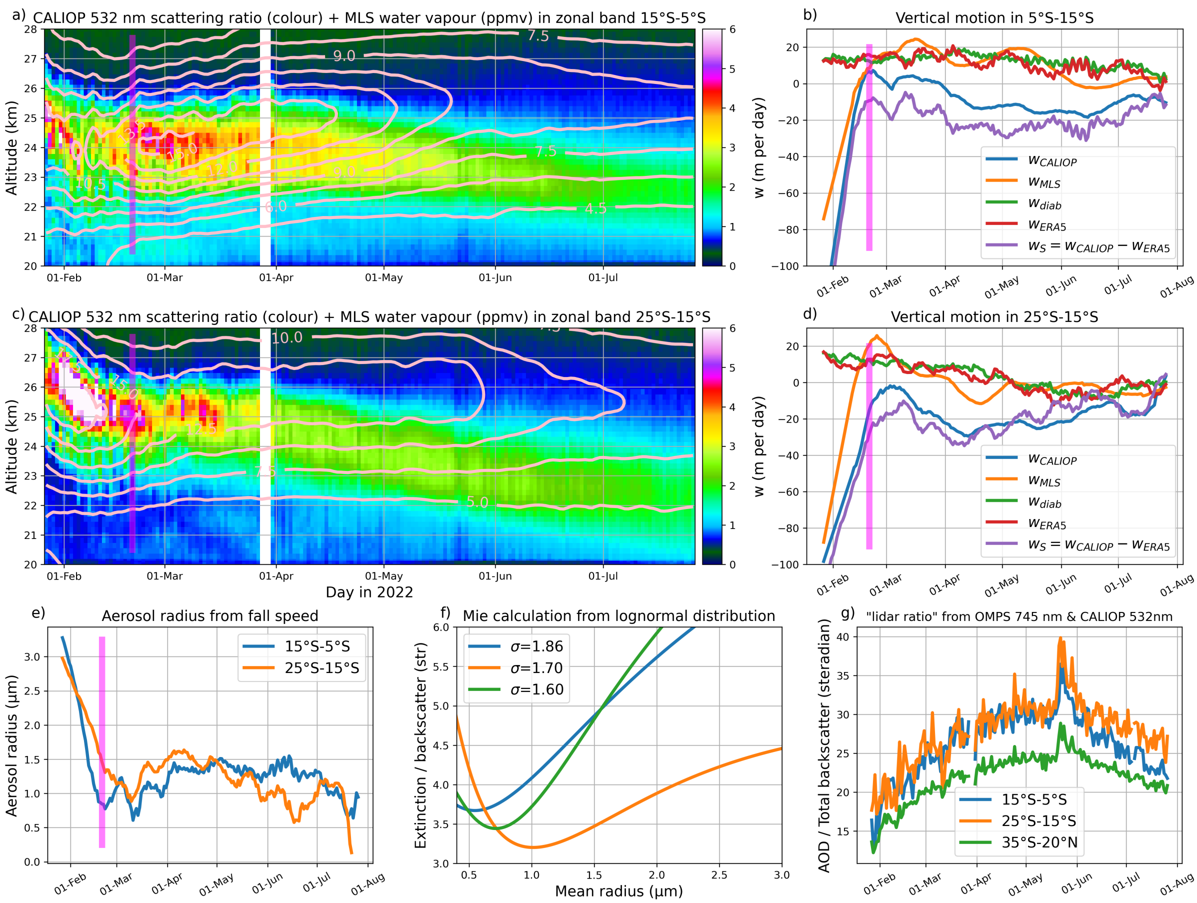

Figure 2. (a) and (c) Zonal and latitude band averages as a function of time for CALIOP 532 nm scattering ratio (colour) and MLS water vapour (contours, ppmv) for, respectively ~~5~~15°~~-15~~S-5°S and ~~15~~25°~~-25~~S-25°S latitude bands. (b) and (d) Vertical motions for the same two latitude bands: ~~W_C~~ W_{CALIOP} for aerosol plume and ~~w_{MLS}~~ W_{MLS} for water vapour plume deduced from ~~(~~a) and ~~(~~c), ~~w_R~~ W_{diab} and ~~w_{adiab}~~ W_{ERA5} for ERA5 diabatic and total (diabatic + adiabatic~~vertical motion~~) ascent rates, and $W_S = W_{\mathrm{CALIOP}} - W_{\mathrm{ERA5}}$ for the resulting vertical motion of the ~~aerosols~~ aerosol plume with respect to the ERA5 air (e) Aerosol radius deduced from w_S interpreted as aerosol fall speed and using Eq. (9.42) of Seinfeld and Pandis (2016). (f) Ratio of the theoretical 745 nm aerosol extinction and 532 nm aerosol backscatter cross sections, calculated using a Mie code (see Appendix A4) with three values of the standard deviation σ. (g) Ratio of the 745 nm OMPS LP aerosol optical depth and 532 nm CALIOP integrated attenuated backscatter, both over the range 18 to 30 km. The curves are shown for the same latitude bands as in a) and c) and for band 35°S-20°N that encompasses also the periphery of the aerosol plume. In panels (a-e), a vertical line is drawn on 20 February to indicate the separation between the two phases of the vertical motion as discussed in Sec. 2.

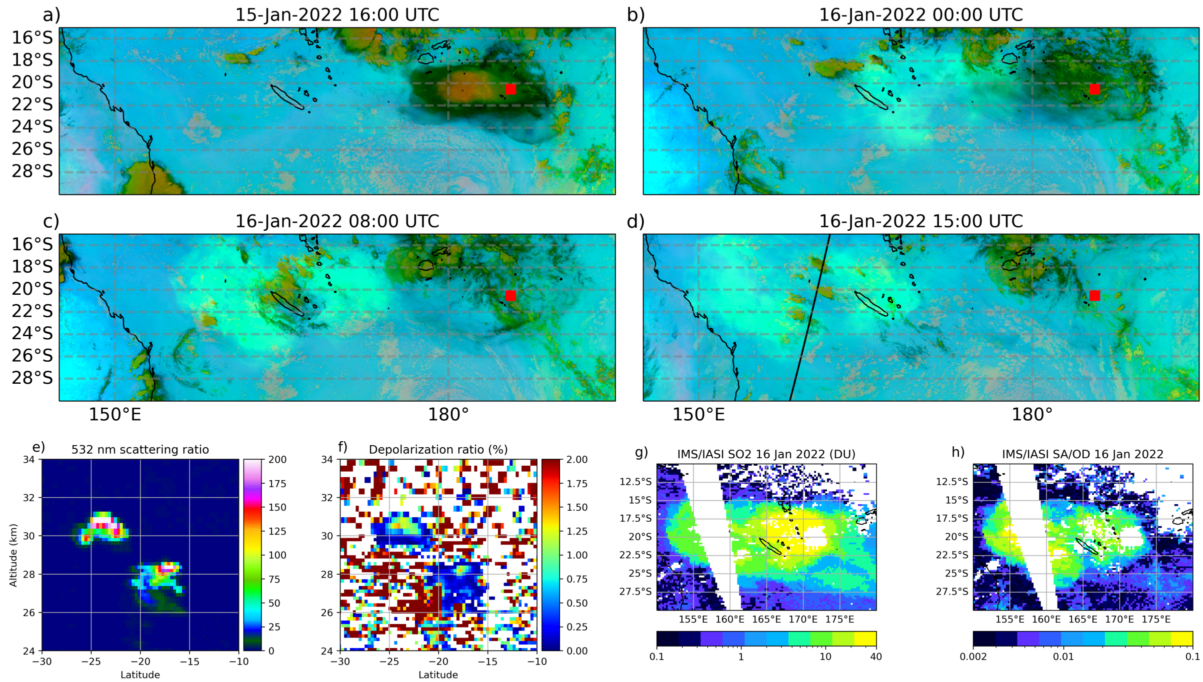

Figure 3. (a-d) RGB-Ash composite (see Appendix A1.6) from Himawari-8 at four selected times during the first day and half following the eruption. The red square denotes the location of the volcano. This product allows to qualitatively distinguish thick ash plumes or ice clouds (brown), thin ice clouds (dark blue) and sulphur-containing plumes (green). Mixed ash/sulphur-containing volcanic species would appear in reddish and yellow shades. (e) CALIOP 532 nm backscatter ratio along the orbit track shown in ~~(~~d) at 15:08 UTC. (f) 532 nm depolarization ratio (orthogonal channel / total) for the same orbit. (g-h) SA/OD and SO_2 from IMS on 16 ~~/02/20222~~ January 2022 for two night orbits crossing the equator at 10:26 UTC (right swath) and 12:08 UTC (left swath).

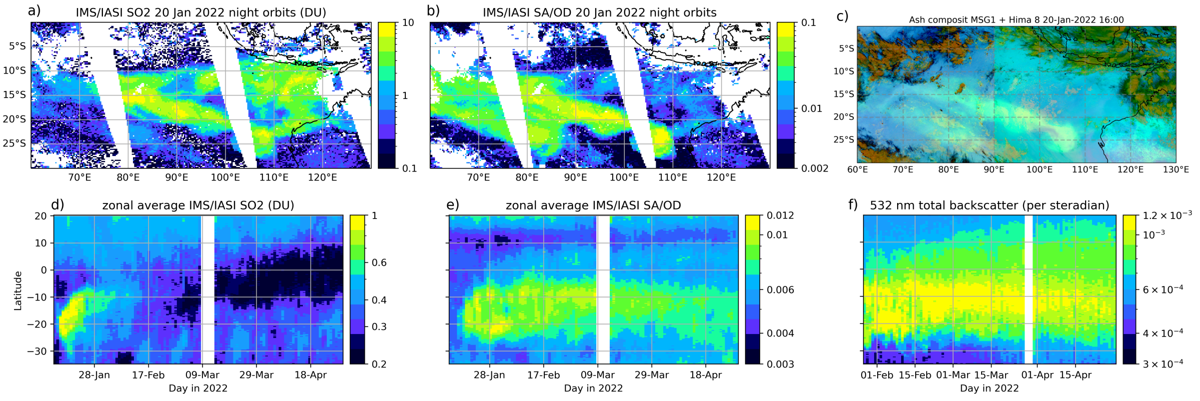

Figure 4. (a-b) SA/OD and SO_2 from IMS on 20 ~~/01/~~January 2022 for three night orbits crossing equator at 14:06 UTC (right swath), 15:48 UTC (middle swath) and 17:29 UTC (left swath). (c) RGB-Ash composite from Meteosat-8 and Himawari-8 at 16:00 UTC on the same day. (d-e) Zonal average SA/OD and SO_2 from 13 ~~/01/~~January 2022 to 30 ~~/04/2022~~ April 2022. (f) CALIOP 532 nm attenuated backscatter integrated between 18 and 30 km from 27 ~~/01/~~January 2022 to 30 ~~/04/~~April 2022 (~~in~~ per steradian).

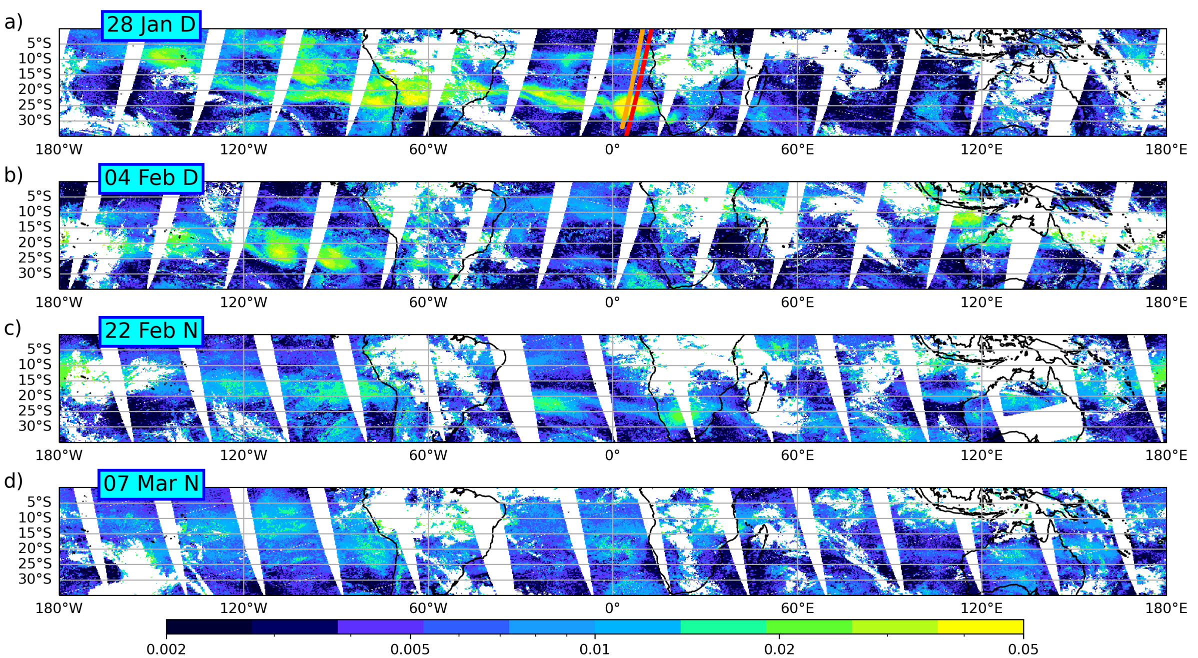

Figure 5. SA/OD from IMS in the latitude range 0°-35°S at four different dates as indicated. Panels ~~a and b~~ (a-b) are drawn for ~~night~~ day swaths ~~while~~ whereas panels ~~c and d~~ (c-d) are drawn for ~~day~~ night swaths. The time progresses from right to left and the interval between two adjacent swaths is 1h52.

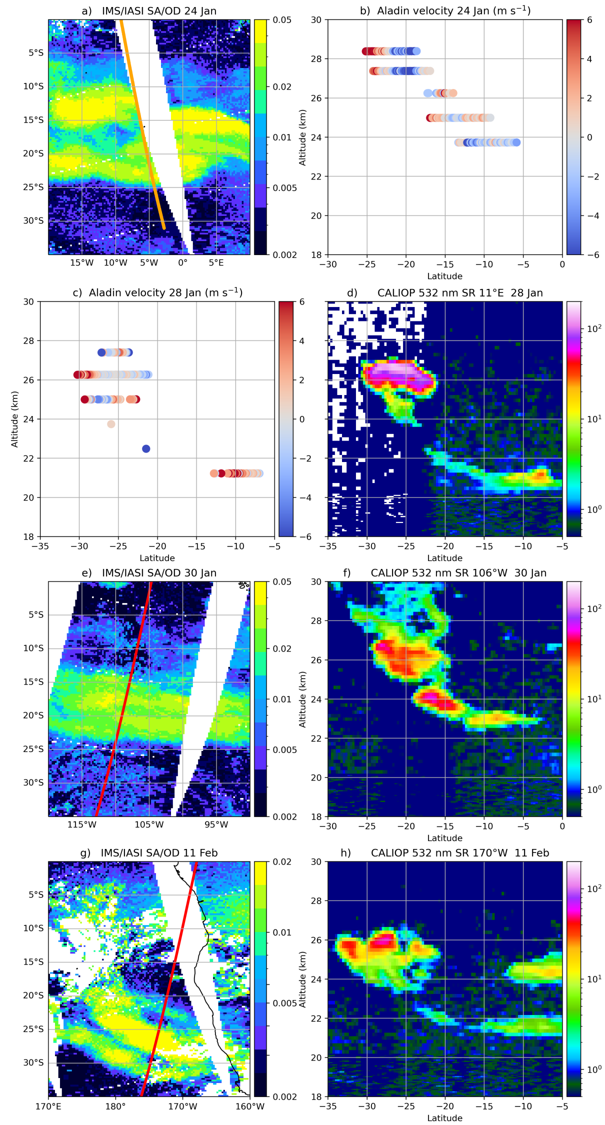

Figure 6. (a) IMS SA/OD chart on 24 January 2022 near 22:52 UTC for the left swath. (b) ALADIN wind anomaly on 24 January 2022 near 18:36 UTC along the track shown in panel a). (c) ALADIN wind anomaly near 5:12 UTC on 28 January 2022 along the the orange track shown on Fig. 5a within the IASI 8:48 UTC swath on the same day. (d) CALIOP ~~522~~ 532 nm scattering ratio on 28 January 2022 near 1:48 UTC along the red track on Fig. 5a. (e) IMS SA/OD chart on 30 January 2022 near 11:28 UTC for the left swath. (f) CALIOP 522 nm scattering ratio on 30 January 2022 near 9:37 UTC along the red track on panel e). (g) ~~Same as e) for~~ IMS SA/OD chart on 11 February near 9:49 UTC for the left s. (h) ~~Same at f) for~~ CALIOP 522 nm scattering ratio on 11 February near 13:52 UTC ~~and~~ along the red track on panel g).

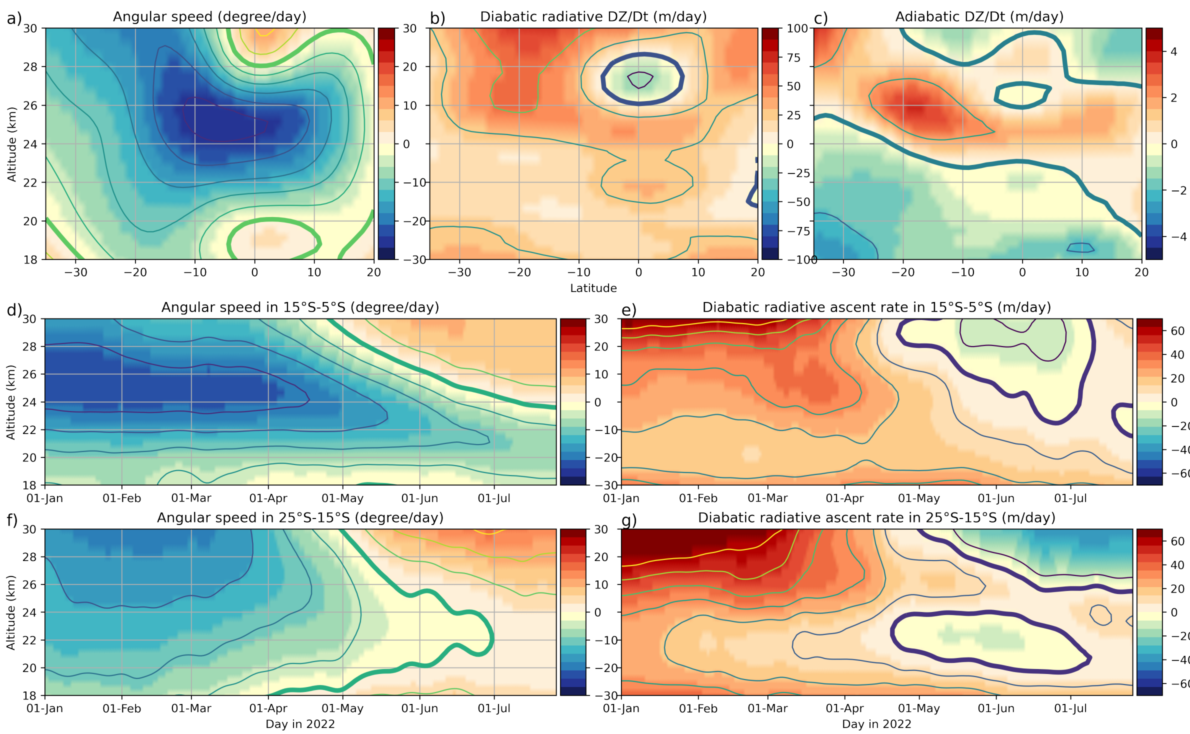

Figure A1. (a) Zonal mean angular rotation speed $\omega = \frac{U}{R_{\mathrm{Earth}}\cos(\phi)}$ from ERA5 averaged between 15 ~~/01/~~January 2022 and 15 ~~/03/~~March 2022 (in $\mathrm{degree\ day}^{-1}$). (b) Same for the diabatic ascent calculated from the total all-sky ERA5 heating rate (in $\mathrm{m\ day}^{-1}$). (c) Same for the adiabatic ascent due to motion of the isentropic surfaces with respect to the geopotential surfaces (in $\mathrm{m\ day}^{-1}$). (d) Daily zonal and altitude band average angular speed between ~~5°~~15°S and ~~15°~~5°S as a function of time (in $\mathrm{degree\ day}^{-1}$). (e) Same as d) for the diabatic ascent (in $\mathrm{m\ day}^{-1}$). (f-g) same as ~~(~~d-e) for the latitude band between ~~15°~~25°S and ~~25°~~15°S.

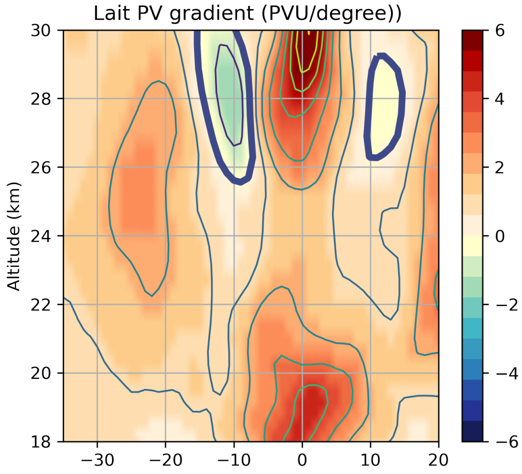

Figure A2. Meridional gradient of the zonal and time average Lait PV defined in Appendix A2. The unit is PVU per degree where 1 PVU = $10^6 \mathrm{m}^2 \mathrm{s}^{-1} \mathrm{K} \mathrm{kg}^{-1}$.